Metal Rod-Based Field Concentrated Common and Differential Modes Theory Enabling Design of Dual-Polarized Antennas

Taeyeong Yoon, *Graduate Student Member, IEEE*, and Jungsuek Oh, *Senior Member, IEEE*

***Abstract*— This article introduces a logical design approach, grounded in an updated understanding of common mode (CM) and differential mode (DM) theory, for the development of dual-polarized antennas operating in the sub-6-GHz N78 band (3.3–3.8 GHz). Our method entails a sophisticated design process that uses the field concentration to achieve the condition of the mode segmentation of *S*-parameters. Notably, enhanced port isolation between the two orthogonal polarizations is accomplished by employing independently controllable Smith chart traces for each mode, utilizing intuitive techniques based on loading metal rods. To offer a comprehensive understanding of the underlying mechanisms that enable the dual-polarized antenna's realization, we present the associated field distributions derived from the CM and DM analyses. The suggested antenna has undergone simulation, fabrication, and measurement processes. Both simulated and experimental findings demonstrate that the antenna can achieve the maximum isolation of 40 dB, an 8-dBi gain, 35-dB cross-polarization discrimination, 90% efficiency with stable radiation patterns, and a $0.14\lambda_0$ profile throughout the 3.3–3.8-GHz range employing cost-effective FR-4 substrates. Moreover, this study contributes a design methodology for dual-polarized antennas, as well as furnishing the active *S*-parameters for a comprehensive range of amplitude and phase sequences to represent realistic situations accurately.**

***Index Terms*— Common mode (CM) and differential mode (DM), decoupling, dual-polarized antenna, isolation, low cost, metal rod loading, mode segmentation.**

I. Introduction

LATELY, fifth-generation (5G) technology has emerged as a prominent subject and rapidly evolved to attain increased data rates and reduced latency, thanks to the vast signal processing demands of wireless communication systems [1], [2], [3], [4], [5]. As a crucial technology in 5G systems, dual-polarized antennas are increasingly sought to boost data throughput in progressively space-constrained application contexts, including base stations, radars, and satellites. Due to these benefits and the wide-ranging demands of different applications, dual-polarized antennas have been the subject of extensive research and development. The N78 band (3.3–3.8 GHz) has been designated for sub-6-GHz 5G new radio in numerous countries, as the advanced system can deliver performance 100 times faster than 4G-LTE and ensure a remarkable latency of less than 1 ms. The emergence of the 5G new radio has spurred considerable interest in the 3.5-GHz band, leading to numerous successful trials as a potential option for base station antennas [6], [7], [8]. Furthermore, the significance of 5G lies in its ability to facilitate vehicle-to-everything (V2X) communication and the Internet of Things (IoT), as it aids in establishing connections that assist drivers on the road [9], [10], [11].

In order to actualize the technology as mentioned above, various techniques have been suggested to enable independent operation by reducing the coupling between two ports of orthogonal polarizations. Among the documented strategies for attaining dual-polarized features and sufficient bandwidth, the most effective methods have included differential L-probe feeder with balun [12], modified feeding lines [13], [14], metasurfaces [15], [16], slot coupled [17], suspended parasitic component [18], [19], cavity-like structure [20], bow-tie dipole [21], [22], magnetoelectric dipole [23], and differentially driven patch with open-loop resonators [24], [25]. In the study referenced as [18], the impedance bandwidth for both ports met the N78 band requirements, exhibiting $|S_{11}| > 10$ dB, by positioning a parasitic metal rod at the radiator's center. Concurrently, the design achieved $|S_{21}| > 25$ dB and cross-polarization discrimination (XPD) > 20 dB. However, this article has the disadvantage of optimizing the alignment of the intermediate metal rods to 0.1-mm increments, which means that measurement error could be significant, and the parametric study that defines the value of S_{21} is unclear. Employing differential coupling cancellation through a balun, the differentially driven antenna in [12] attained high port isolation across an extensive frequency range, sustaining $|S_{11}| > 10$ dB, $|S_{21}| > 20$ dB, and XPD > 20 dB. Nonetheless, neither of these investigations addressed the coupling issue, which is essential for realistic environmental conditions between the ports, meaning that they did not provide results for active *S*-parameters. Hence, in this article, we examine an active *S*-parameter analysis that incorporates the coupling impact on the matching condition for each port, covering all feasible amplitude and phase configurations. Furthermore, in [26],

Manuscript received 22 March 2023; revised 28 June 2023; accepted 15 July 2023. Date of publication 1 August 2023; date of current version 6 October 2023. This work was supported by the Institute of Information and Communications Technology Planning and Evaluation (IITP) Grant funded by the Korean Government [Ministry of Science and ICT (MSIT)], Innovative Fusion Technologies of Intelligent Antenna Material/Structure/Network for THz 6G, under Grant 2021-0-00763. *(Corresponding author: Jungsuek Oh.)*

The authors are with the Department of Electrical and Computer Engineering (ECE), Institute of New Media and Communications (INMC), Seoul National University, Seoul 151-742, Republic of Korea (e-mail: taeyeong.yoon@snu.ac.kr; jungsuek@snu.ac.kr).

Color versions of one or more figures in this article are available at https://doi.org/10.1109/TAP.2023.3299008.

Digital Object Identifier 10.1109/TAP.2023.3299008

a suitable isolation level for multiple antennas was established based on an active impedance analysis, the concept of which was introduced in [27]; this condition and scenario can be deemed analogous to the design of dual-polarized antennas. Consequently, drawing from the reference, we set the isolation level objectives at >20 dB.

The present study extensively utilized the theory of common mode (CM) and differential mode (DM), as outlined in [28], for the design of couplers and power dividers. By employing structural symmetry, the complexity of the analysis was reduced, resulting in reliable outcomes. Recently, techniques boasting these advantages have been actively explored for application in the propagation domain [29], [30], [31], [32], [33]. In [30], the CM and DM theory was proposed to eliminate mutual coupling between two antenna elements. Specifically, methods for improving the isolation performance of dipole and planar inverted-F antennas were introduced and examined based on the CM and DM theory. In addition, in [31], decoupling was achieved through the use of a defected ground structure, along with CM and DM analysis between microstrip patch antenna elements. In [32], isolation was accomplished by employing a connected line between slot antennas, which was made possible by conducting an innovative analysis while maintaining symmetry through the introduction of a new structure. As these characteristics are important in dual-polarized antennas, this article focuses on the CM and DM analysis of dual-polarized antenna design.

In this study, we propose a straightforward and practical design approach grounded in a new perspective on CM and DM analysis. In our method, the isolation between two symmetrically structured ports is theoretically equivalent to the impedance matching of the CM and DM. Consequently, the unique and evident field properties of the CM and DM can aid in understanding the coupling issue and attaining port isolation by independently adjusting CM and DM impedances. When a similar impedance state for CM and DM is achieved near 50 Ω, the coupling current produced by the shared radiator between the two ports in the passive antenna element can be entirely eliminated, and the matching condition can be maintained through the superposition of CM and DM. To validate the viability of this technique, we present a practical design example that includes mutual coupling reduction between each port of the dual-polarized antenna. The design example illustrates that the proposed method can provide a systematic design guideline, a simplified and structured design process, and satisfactory port isolation performance. The key innovations of this study can be summarized as follows.

1) We propose an in-depth perspective on dual-polarized antenna design, which allows for a high hierarchy design than the traditional analysis of field distributions; Smith charts' trajectory optimization for CM and DM modes is introduced to overcome a simple parametric study for performance optimization.
2) Metal rods have been incorporated to enable independently controllable Smith charts for CM and DM, achieving the desired field distribution and also functioning as a jig. Consequently, this antenna does not require the jig, which is used in the conventional antenna, even with an air-filled substrate. In addition, the independent trace of CM is realized through the voltage null of differential ports, while DM is attained by maintaining a similar CM field but with a changed DM field.
3) This article proposes an optimization approach to minimize the matching degradation of active *S*-parameters in moderate isolation levels at the edge of the target frequency band.
4) Employing FR-4 substrates allows for low-cost antenna fabrication. Furthermore, high efficiency (90%) is achieved by using metal rods to create an air-filled substrate, despite the highly lossy substrate utilized in the antenna design.

The structure of this article is organized as follows. Section II introduces the CM and DM theory for sophisticated antenna design. In Section III, we provide a design example of the dual-polarized antenna, complete with detailed design guidelines and antenna performance. Section IV offers a new perspective on performance comparison, including the mutual coupling effect, through an active *S*-parameters analysis. Finally, Section V presents the conclusions derived from this research.

II. Principle of the CM and DM Theory

Fig. 1 shows a sketch diagram of a generic dual-polarized antenna system. As a dual-polarized antenna, the ports are designed to generate orthogonal currents for each path. The red and blue arrows in Fig. 1 indicate the currents of each port. The objective of a dual-polarized antenna, widely recognized, is to attain a single-ended and passive *S*-parameter of $S_{21} = 0$, enabling independent operation and improved data throughput. Interestingly, notably, this can be achieved through the utilization of the CM and DM theory, and the analysis methodology introduced in this research. CM and DM denote the application of in-phase and out-of-phase signals, respectively, to each port in the two-port antenna system. Hence, in CM, identical phases and power are generated at each port, and the boundary at the center between the ports becomes a perfect magnetic conductor (PMC). In DM, similar to CM, the power applied to each port is the same, but the phase difference is 180°, and the potential becomes zero at the center between the ports, resulting in a perfect electric conductor (PEC) boundary [28]. The dual-polarized antenna system's CM and DM *S*-parameters are provided in [34]. The equations presented in previous publications were formulated for individual radiators, representing separate antennas. In contrast, this article employs the aforementioned equations to analyze a shared radiator.

In particular, due to the symmetrical and reciprocal two-port network of the proposed dual-polarized antenna, the equations fulfill the conditions $S_{11} = S_{22}$ and $S_{12} = S_{21}$. Consequently, the CM and DM *S*-parameters for a dual-polarized antenna system can be simplified as follows:

$$S_{11} = S_{22} = (S_{CM} + S_{DM})/2 \tag{1}$$

$$S_{21} = S_{12} = (S_{CM} - S_{DM})/2. \tag{2}$$

From (1) and (2), it is evident that the isolation equation of $S_{21} = 0$ between the ports can be realized for $S_{CM} = S_{DM}$

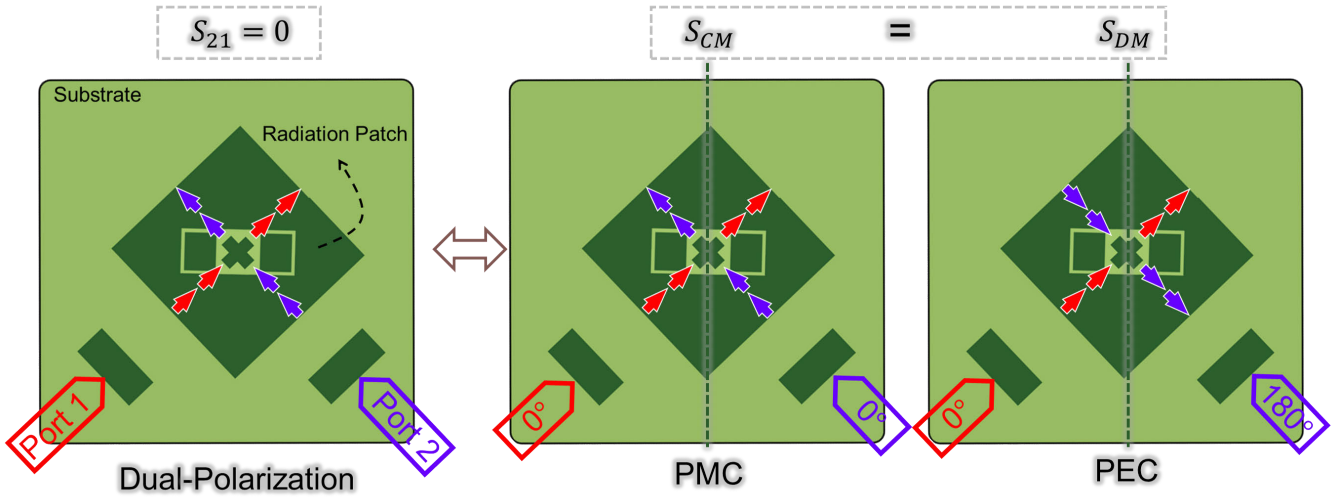

Fig. 1. Schematic of a dual-polarized antenna and the associated current distributions on the radiating patch.

when considering the design of the dual-polarized antenna from the standpoint of the CM and DM theory. In other words, for any symmetrical and reciprocal dual-polarized antenna, if the CM and DM *S*-parameters are equal, successful isolation between the ports can be achieved. Moreover, if the CM and DM *S*-parameters are close to 50 Ω, the matching condition is also satisfied. This conclusion offers new insights into the design of dual-polarized antennas, which will be discussed in more detail in Section III.

In the following, an independently adjustable CM and DM theory-based approach for a more straightforward and logical design is presented, beginning with the design and determination of antenna dimensions in the target frequency band. Metal rods are employed to enable the current concentration and the air-filled substrate to satisfy the N78 band requirements. Contrary to other studies, this method implements an air-filled substrate and allows the antenna to function without an additional jig for stabilization. Furthermore, the desired field is achieved through structural modifications using metal rods, resulting in an independently controllable performance for CM and DM analysis.

III. Design of the Dual-Polarized Antennas

The development of the dual-polarized antenna and its design parameters are shown in Fig. 2, displaying the top and side views. As shown in Fig. 2(a), an air-filled substrate and indirect feed were employed to secure ample bandwidth, meeting the N78 band requirements. By using an air-filled substrate, a suitable bandwidth could be attained via (3) from [35]

$$BW = \frac{96h\sqrt{\mu/\varepsilon}}{\lambda\sqrt{2}(4 + 17\sqrt{\mu\varepsilon})} \tag{3}$$

where ε and h are the permittivity and the thickness of the substrate, respectively. In order to improve the antenna bandwidth, it is necessary to use a substrate that is both thick and has low permittivity. However, standard substrates typically have a thickness and permittivity greater than 1, which limits the bandwidth of many antennas. To overcome this limitation, air-filled substrates with a permittivity of 1 can be used. Metal rods were employed on two sides of the substrate to achieve an air-filled substrate, as shown in Fig. 2(a), as they not only excite the patch but also fix the upper substrate. A coplanar capacitive feeder was used with the rods connected by a via hole. While using an air-filled substrate provides performance advantages, it can also increase process complexity. In addition, rectangular copper traces were added to the upper substrate, as shown in Fig. 2(a), to indirectly excite the patch for improved bandwidth [36]. To control each mode, steps 1 and 2 were proposed as shown in Fig. 2(b) and (c), where the slot and metal rod were employed to concentrate the electric field effectively. The dimensions of the slot and the presence of the middle metal rod were important factors to consider, as the field can be weak if the slot is too big or the middle metal rod is absent. Fig. 2(b) shows a cruciform slot, and the middle metal rod is connected to the metal layer of the upper substrate via a via hole (see side view). Similarly, Fig. 2(c) has additional metal patterns and rods around the cruciform pattern.

A. Design Procedure

To ensure proper antenna operation, it is essential to have adequate bandwidth and matching. Hence, a parametric study was performed, as shown in Fig. 3, to investigate the effect of various design parameters. It is desirable to have a higher value of $|S_{11}|$ for better matching, as it can easily be affected by coupling. Furthermore, the independent mode results were presented by adjusting the l_2 parameter, which corresponds to the electric field added only in CM, and s_p, which corresponds to the electric field added only in DM. Fig. 3(a) shows the results when the width of the feeder of the antenna is adjusted. This method changes both poles and was used to set the center frequency. Narrower width decreases the frequency of the pole in the lower band and increases the frequency of the upper band. Fig. 3(b) shows the results after adjusting the distance between the indirect feeder and the radiator. The frequency of the poles is maintained, but the isolation level changes reversely. This method was used in

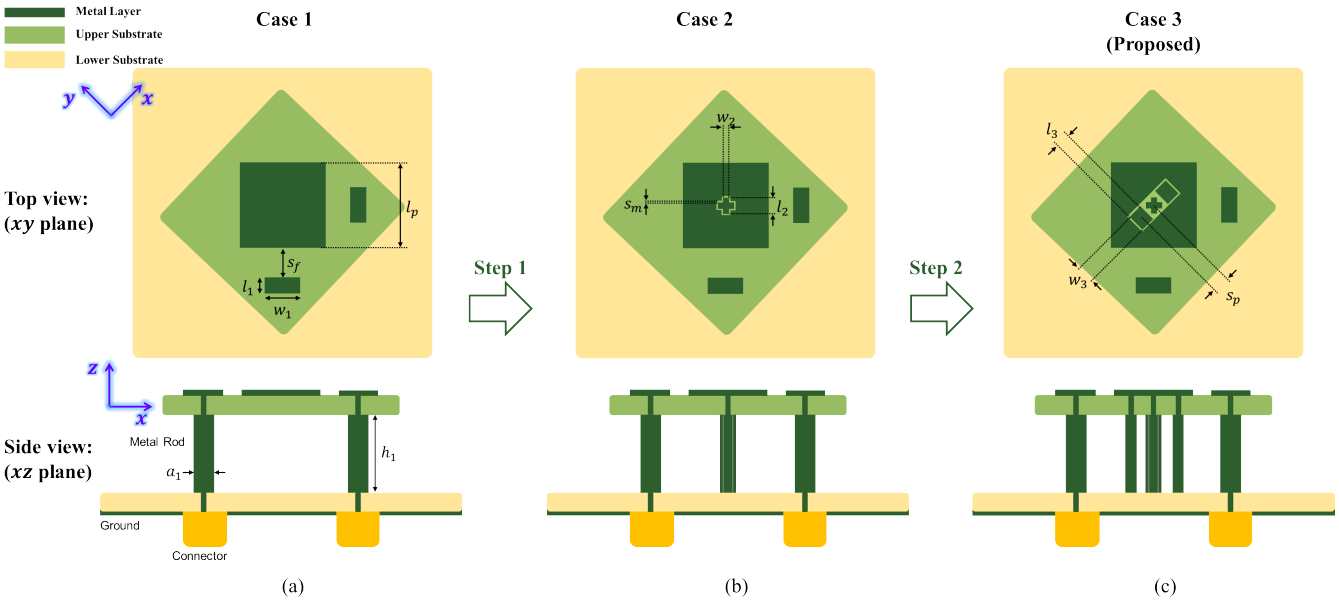

Fig. 2. Progression of the top and side views of the dual-polarized antenna, where $w_1 = 3$ mm, $l_1 = 3$ mm, $s_f = 4$ mm, $l_p = 22$ mm, $a_1 = 2$ mm, $h_1 = 9.5$ mm, $s_m = 0.4$ mm, $w_2 = 1$ mm, $l_2 = 3$ mm, $w_3 = 2.6$ mm, $l_3 = 2$ mm, $s_p = 3$ mm. (a) Case 1: dual-polarized antenna without decoupling structures. (b) Case 2: with the cruciform metal rod and slot for independently controllable CM only. (c) Case 3 (proposed): with the additional metal rods and a slot for both independently controllable CM and DM.

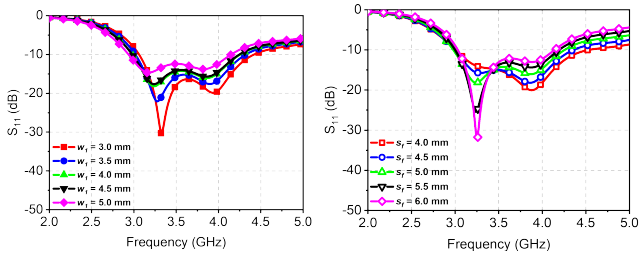

Fig. 3. Simulated reflection coefficient results concerning various antenna geometry parameters. (a) Results for different widths, w_1. (b) Results for different values of the distance between the feeder and radiator s_f.

the optimization process to achieve $|S_{11}| > 10$ dB and robust matching conditions for coupling effects. To minimize the degradation of impedance bandwidth by the coupling effect, the two poles should be placed at each side of the frequency band, i.e., 3.3 and 3.8 GHz. In addition, two thin FR-4 substrates (thickness = 1.6 mm) were used, with the upper substrate laminating the coplanar feeding network and the radiation patch, whereas the lower substrate was used for the ground and connectors. A low-cost method was implemented using this typical process. The CM and DM analysis was used to design for isolation between the ports by performing the following two steps.

Step 1: A floating metal rod in a cruciform shape was inserted in the center of the radiation patch, as shown in Fig. 2(b). The additional metal rod did not change the electrical field distribution for the DM because of the PEC boundary condition that created a zero voltage difference in the middle of the patch. This is shown in Fig. 4(a) and (b), where the DM Smith chart remains constant. However, the electrical field distribution of the CM changed due to the additional structure, allowing for independent control of the CM Smith chart. As a result, the trace of the CM Smith chart could be adjusted independently, while the trace of the DM remained unchanged, as shown in Fig. 5(a) and (b) for different values of l_2.

Step 2: Metal rods were placed closer to the center rod in Fig. 2(c), resulting in an additional structure with a strong electric field distribution for the DM next to the middle metal rod, as shown in Fig. 4(c), because the region is not a PEC boundary. However, the electrical field distribution was similar to that in case 2 next to the extra metal rod close to the middle one, leading to a constant CM Smith chart. Thus, the further metal rods near the middle one could independently adjust DM impedance, while the CM impedance remained unchanged, as shown in Fig. 6(a) and (b) for different values of s_p. Consequently, the Smith chart for each mode was realized, as shown in Fig. 7, and isolation was achieved at 3.5 GHz (crossing point).

Fig. 8(a) shows the isolation and reflection coefficient results. As mentioned earlier, optimizing S_{11} is important, achieved by positioning the poles at the edge of the frequency band. This is necessary because the isolation level at the band's side, specifically at 3.3 and 3.8 GHz, is relatively low. Specifically, the level of $|S_{11}|$ should be higher at 3.8 GHz compared to 3.3 GHz, as the isolation level at 3.8 GHz is lower than at 3.3 GHz. This consideration is crucial in maintaining impedance matching and accounting for coupling effects when dealing with an active S-parameter. This is achieved through optimization based on Fig. 3(b). It is important to note that optimization is easily achieved since the dimension control for the matching condition does not affect S21, as shown in Fig. 8(b), because an independently adjusted field realized it. In other words, the control parameters for S_{11} and S_{21} are independent.

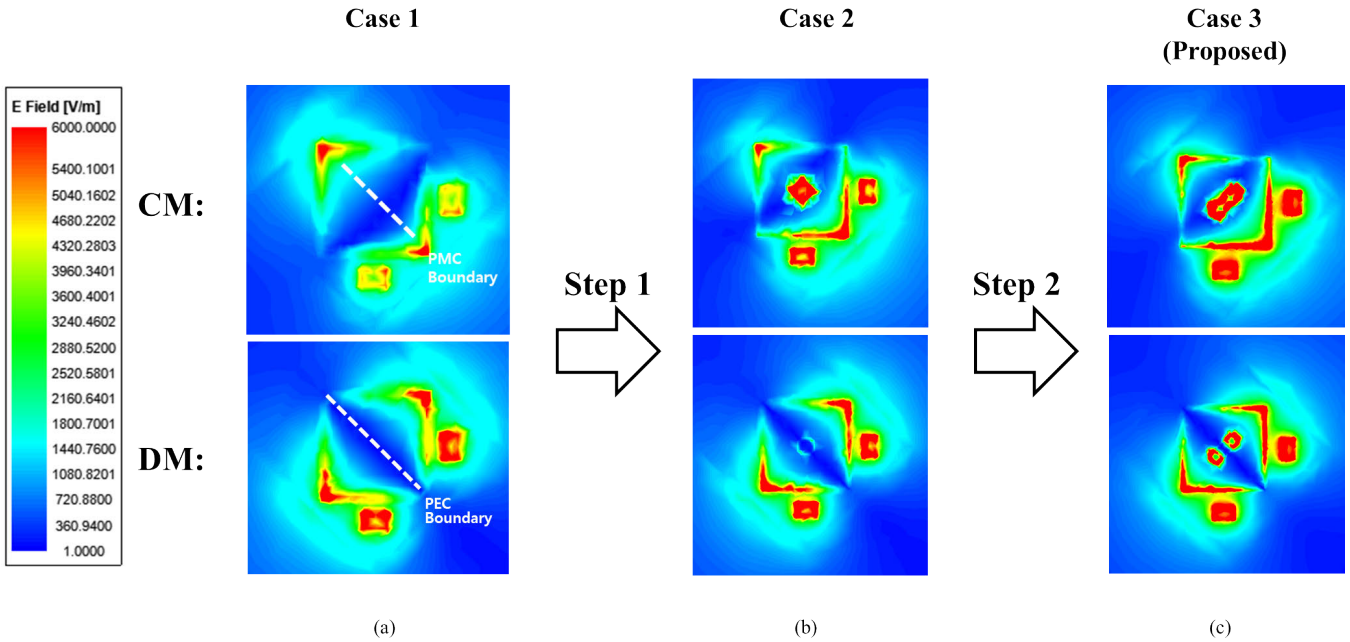

Fig. 4. Electrical field distributions for CM and DM in (a) Case 1, (b) Case 2, and (c) Case 3 (proposed).

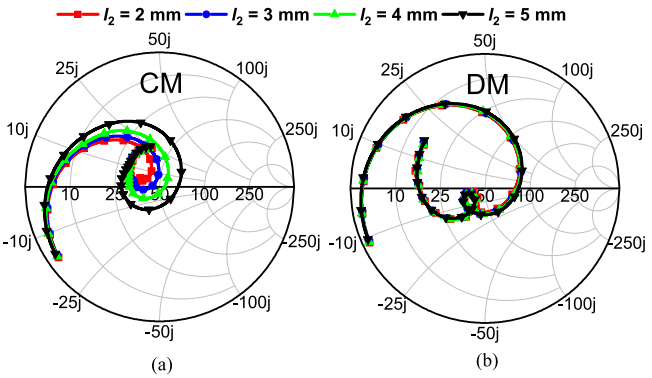

Fig. 5. Smith charts of Case 3 under various values of l_2 for (a) CM and (b) DM.

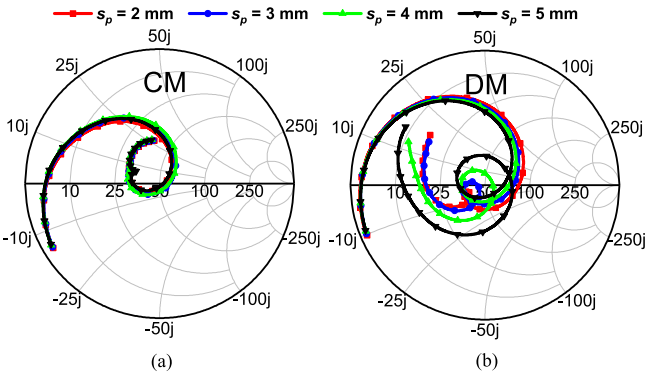

Fig. 6. Smith charts of Case 3 under various values of s_p for (a) CM and (b) DM.

To investigate the effect of metal rod loading, the metal rod inserted for isolation was removed, as shown in Fig. 9(a), and its impact was analyzed. Fig. 9(b) shows the isolation results with and without the metal rod, indicating metal rod loading enhanced isolation. The electrical field distributions

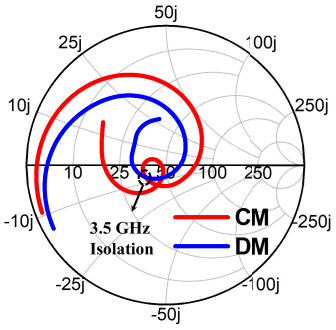

Fig. 7. Smith charts realizing isolation for Case 3 from independently controlling each mode.

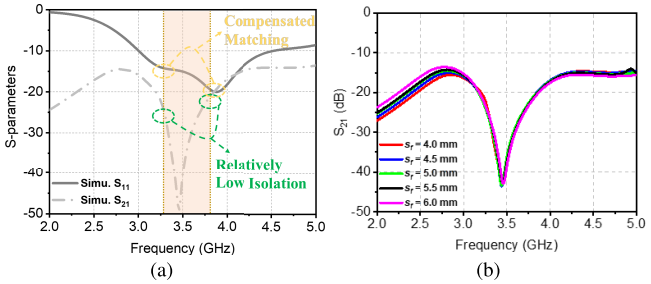

Fig. 8. Simulated S-parameter results: (a) with the compensated matching to overcome the isolation degrade and (b) with respect to different spacing, s_f.

shown in Fig. 10(a) and (b) explain this phenomenon. The metal rod effectively collected charges over a large volume, which disappeared when the metal rod was removed, leading to low coupling and weak field concentration.

B. Experimental Results

A prototype of the proposed dual-polarized antennas was manufactured to demonstrate their performance, as shown in

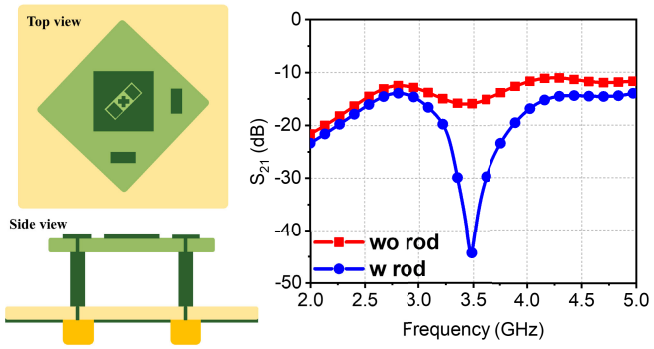

(a) (b)

Fig. 9. Illumination of Case 3 without metal rods: (a) top and side views and (b) results for the presence of the rod.

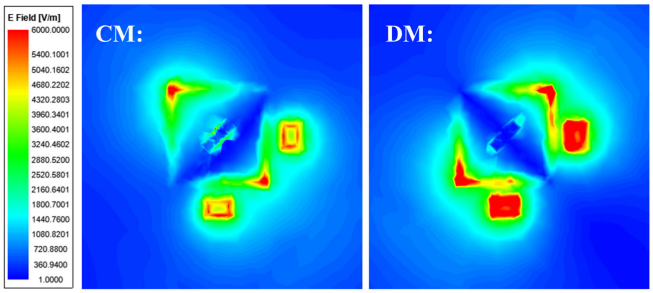

(a) (b)

Fig. 10. Electrical field distributions for Case 3 without the rod. (a) CM. (b) DM.

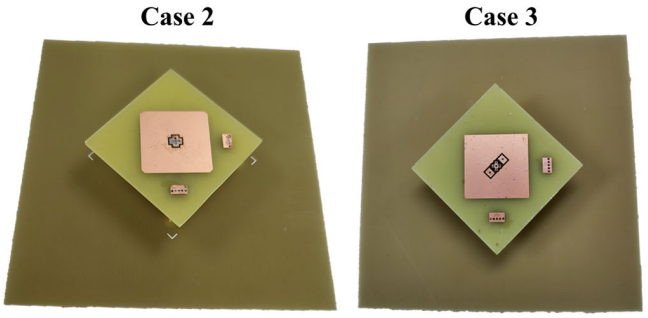

(a) (b)

Fig. 11. Photograph of the presented dual-polarized antenna corresponding to (a) Case 2 and (b) Case 3 (proposed).

Fig. 11(a) and (b). The two FR-4 substrates were connected by soldering metal rods, and two 50-Ω SMA connectors were used for the antenna test. The measured results for *S*-parameters according to the corresponding cases are shown in Fig. 12(a) and (b). It can be observed that the condition $|S_{11}| > 10$ dB is satisfied from 3.3 to 3.8 GHz in both cases. However, in the absence of the proposed methods, the isolation between the ports is only about 15 dB, as shown in Fig. 12(b). In contrast, by implementing the CM and DM, the isolation is progressively improved. When only the DM is controlled, the isolation reaches 20 dB. When both CM and DM are independently adjustable, the isolation of up to 40 dB is achieved through a more refined design. Therefore, the proposed multifunctional metal rods provide an advanced design methodology for dual-polarized antennas.

The realized gains and efficiencies obtained from both simulations and measurements are shown in Fig. 13(a) and (b),

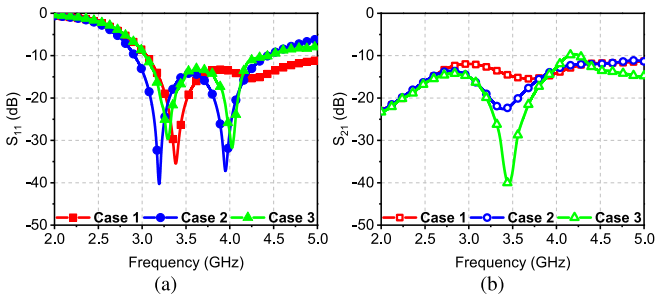

(a) (b)

Fig. 12. Measured results of (a) S_{11} and (b) S_{21} for Cases 1–3.

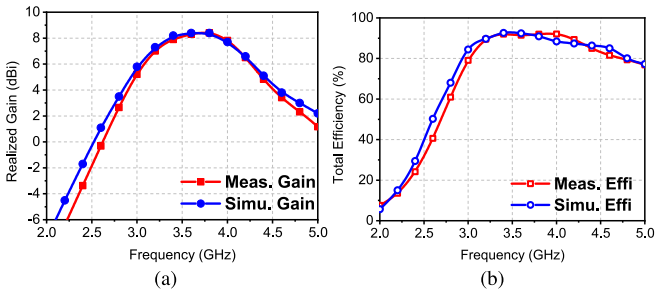

(a) (b)

Fig. 13. Simulated and measured results for Case 3: (a) realized gain and (b) total efficiency of the proposed dual-polarized antenna.

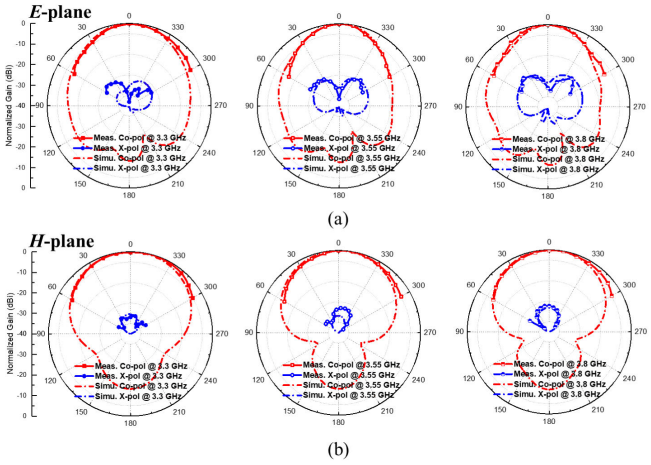

(a)

(b)

Fig. 14. Simulated and measured results for Case 3: (a) E-plane and (b) H-plane at 3.3, 3.55, and 3.8 GHz.

respectively. The simulated realized gain is between 8 and 8.4 dBi across the targeted band (3.3–3.8 GHz), while the measured value remains stable at 8 dBi. Furthermore, the total efficiency simulated ranges from 88% to 92%, whereas the measured value ranges from 90% to 92%. Despite the high loss tangent of the FR-4 substrate, the low loss from the air-filled substrate and the excellent impedance matching contributes to the high performance of the antenna. As a result, both the matching and isolation conditions are satisfied for the N78 band, with the realized gain and total efficiency being approximately 8 dBi and 90%, respectively. Consequently, it is possible to obtain constant value results in the targeted band to achieve the same performance for each frequency.

The normalized radiation patterns for E- and H-planes, obtained by feeding the signal through a port and terminated by a 50-Ω resistance, are presented in Fig. 14(a) and (b), respectively, for both simulated and measured results. The radiation patterns are symmetrical between the two ports and

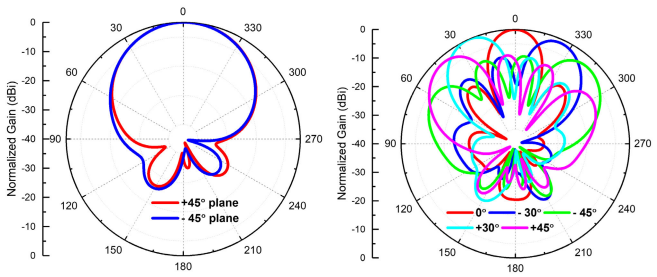

(a) (b)

Fig. 15. Radiation pattern results of (a) diagonal plane and (b) 1 × 4 array beamforming at 3.55 GHz.

have thus not been shown for brevity. From Fig. 14(a) and (b), it can be observed that a pattern with low cross polarization is achieved in the broadside direction from 3.3 to 3.8 GHz, with a maximum of approximately 35 dB at 3.5 GHz. The half-power beamwidth (HPBW) of E-plane, H-plane, and diagonal plane is 28°, 36°, and 30°, respectively. To analyze the capability of beamforming for the antenna, since it is a slant polarized 1 × 4 array, the radiation pattern of a diagonal plane is provided, as shown in Fig. 15(a); Fig. 15(b) reveals that the system offers 45° beamforming. Moreover, the radiation patterns are stable and show good agreement between the simulated and measured results.

C. Design Guide

This section presents a design procedure for symmetric antennas, which can be applied to various applications. As shown in Fig. 16, this procedure can be used not only for designing dual-polarized antennas using the approach proposed in this article but also for other methods, as dual-polarized antennas are commonly symmetrical to achieve uniform performance for both polarizations.

In the design process, the first step was to choose a suitable PCB substrate based on the cost and structural stability. The second step involved selecting the antenna topology and dimensions to meet the bandwidth and center frequency requirements. To efficiently change the electrical field distributions of the antenna, a structural idea was proposed, which employed strong coupling with the slots and floating metal rods for CM and DM theory. For more sophisticated designs, it was essential to find a method that could adjust each mode independently. The PEC boundary was used to control the CM, and by placing an additional structure close to the center, a similar field distribution for the CM could be obtained; a new field distribution was created for DM. Thus, CM and DM could be independently adjusted. Note that this is just one method, and other methods may follow the design procedure shown in Fig. 16. Analyzing the active *S*-parameters at the end of the block in Fig. 16 is important to consider coupling issues in practical situations, which will be addressed in the following.

IV. Intensive Interpretation Considering the Coupling Effect

In this section, a detailed analysis of dual-polarized antennas is presented to reflect the influence of practical requirements

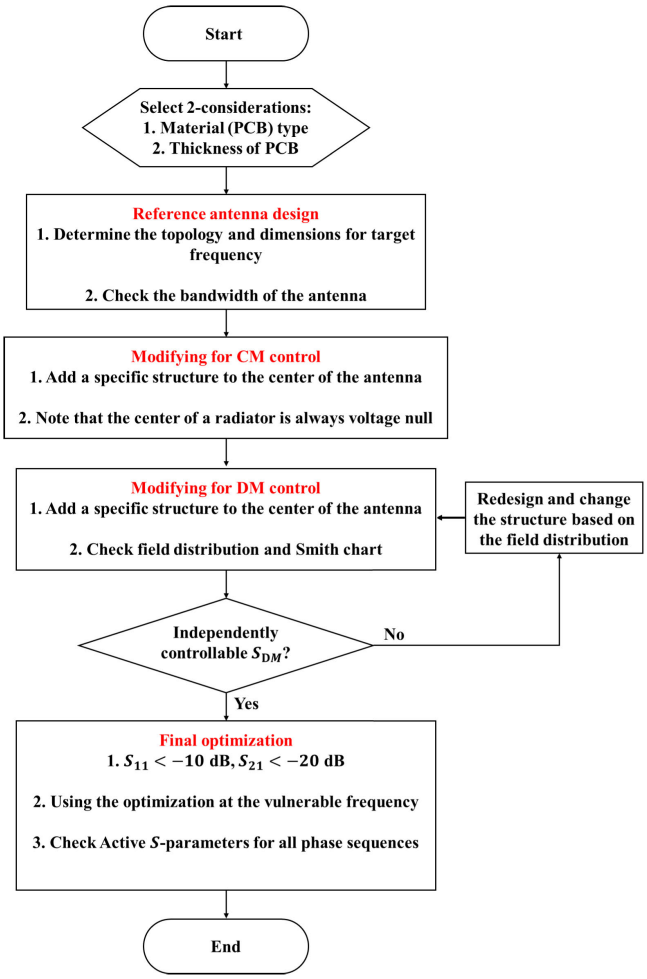

Fig. 16. Flowchart illustrating the design procedure for achieving a symmetric structure.

on the results. Previous studies have only focused on verifying the isolation between the ports using the proposed design methods for dual-polarized antennas. However, since a dual-polarization antenna operates independently, simultaneous operations must be considered. In this study, new issues regarding active *S*-parameters analysis have been introduced by considering the coupling effect. By considering practical conditions, it is expected that the optimal performance for the desired application can be achieved rather than solely evaluating the antenna performance at the *S*-parameter level using the proposed concept.

The active *S*-parameter is calculated as follows [37]:

$$Act.S_{porti} = \sum_{j=1}^{n} S_{ij} \frac{a_j}{a_i} \tag{4}$$

where S_{ij} is the passive (typical) *S*-parameter under terminated conditions. a_j is the complex excitation coefficient of port j, which includes an amplitude and a phase. Since dual-polarized antennas consist of two ports and reciprocal systems, (4) can be modified as follows:

$$Act.S_{port\ 1} = Act.S_{port\ 2} = S_{11} + (\Delta A \times e^{j\Delta\phi}) S_{12} \tag{5}$$

$$\Delta A = \frac{|a_2|}{|a_1|},\ \Delta\phi = \angle a_2 - \angle a_1 \tag{6}$$

TABLE I
PERFORMANCE COMPARISON TABLE

Ref.	Method	Frequency (GHz)	Antenna Size ($\lambda_0{}^3$)	Isolation (dB)	XPD (dB)	Total Efficiency (%)	Gain (dBi)
[14]	Cascaded quadruplet patch	1-1.2 (18%)	0.34×0.34×0.05	> 23	20	90	8
[15]	Vivaldi with metasurface	8-24 (100%)	0.44×0.44×0.81	> 18	20	90	10
[18]	Suspended patch	3.3-3.8 (14%)	0.5×0.5×0.14	> 30	26	-	9
[20]	Cavity-like structure	3.4-3.8 (11%)	0.45×0.2×0.04	> 40	15	87	3
[38]	Magneto-electric dipole	3.3-4.2 (24%)	0.6×0.6×0.09	> 30	25	90	8.2
[39]	Crossed straight dipoles	1.68-2.94 (54%)	0.32×0.32×0.2	> 28	20	-	8.5
[40]	Vector synthesis	3.3-3.6 (8%)	0.29×0.29×0.2	> 26	25	90	8
This work	Mode segmentation using metal rods	3.3-3.8 (14%)	0.32×0.32×0.1	> 21	35	90	8

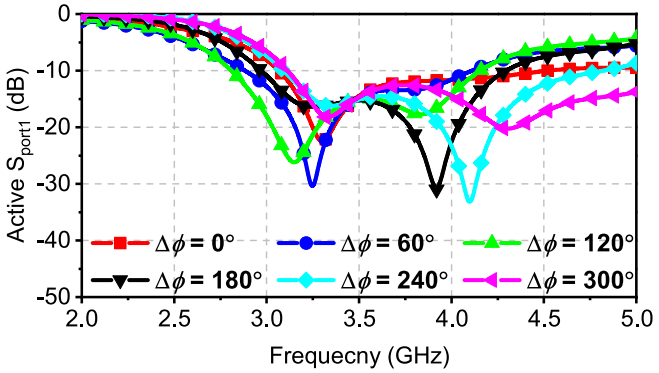

Fig. 17. Measured active S_{port1} for various phase differences with the amplitude ratio as 1.

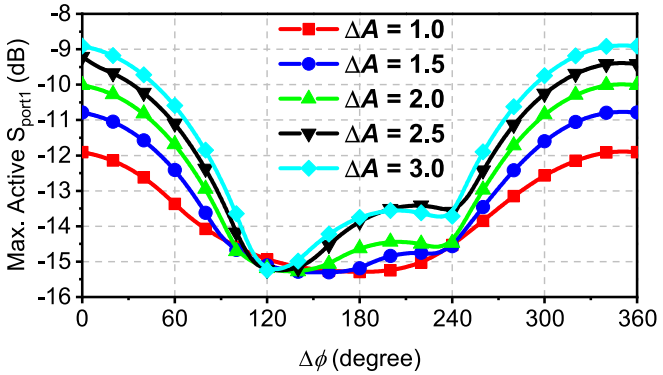

Fig. 18. Measured maximum active S_{port1} from 3.3 to 3.8 GHz considering possible amplitude ratio and phase difference for realistic conditions.

where ΔA and $\Delta\phi$ represent the amplitude ratio and the phase discrepancy between the ports, respectively. As shown in (5), when both ports are excited, S_{11} can be influenced by the amplitude ratio, the phase disparity between the ports, and S_{12}. This can alternatively be construed as a physical understanding. If we consider the matching of two antennas operating independently, the inherent matching conditions and coupling levels affect the result. Moreover, the power and phase of the neighboring element also affect the outcome: as the power escalates, the specific phase leading to the in-phase between S_{11} and S_{21} deteriorates the result.

Fig. 17 shows the alterations in the active S-parameter in port1 when a phase difference is introduced, assuming that the same power is excited to each port with $\Delta A = 1$. Upon examining the results of the aforementioned method and referencing the S-parameter outcomes shown in Fig. 12(a) and (b), it is apparent that the results for distinct values of the phase difference fulfill the matching condition of $|S_{port1}| > 10$ dB from 0° to 360°, taking the coupling effect into account. The impedance bandwidth is maintained, albeit the isolation level remains inadequate, around 20 dB, since the two poles in the impedance bandwidth were positioned on either side of the band. In other words, when equal power is provided between each port, the dual-polarized antenna operates as intended.

Fig. 18 shows that the outcomes of the proposed antenna performance are impacted in situations where ΔA and $\Delta\phi$ change concurrently across 3.3–3.8 GHz in realistic scenarios. Plotting all graphs for each alteration simultaneously would make them difficult to discern and occupy considerable space. As a result, this study specifically opted for identifying the maximum value of the active S-parameter in the N78 band. The x-axis represents the range of the phase difference, and the overlapping graphs with varying ΔA values exhibit the change in the applied amplitude ratio. Consequently, it is evident that as ΔA escalates, the coupling intensifies and the matching level worsens, which can also be inferred from (5). To summarize the analysis, in the proposed dual-polarization antenna, when each port operates autonomously and considering the $|S_{port1}| > 10$ dB matching conditions, the amplitude ratio can be utilized up to $\Delta A = 2$ in all phase difference sequences.

Table I presents a performance comparison of the proposed dual-polarized antenna with other recently published antenna works; the parameters are based on measurement values. In Table I, λ_0 denotes the free-space wavelength at the lowest value of the operating frequency. The proposed antenna displays competitive performance based on the other patch-based antennas; the Vivaldi and cavity structure antennas have advantages when it comes to bandwidth and isolation, while each antenna has a large size and low gain, respectively. It was devised on the basis of a higher hierarchy analysis. Furthermore, despite utilizing an FR-4 substrate, high efficiency and gain were accomplished. The results corresponding to the proposed design in this work are on par with those documented in the literature concerning isolation and XPD values; this method, which is specific to isolation formation, has significant advantages for forming enhanced XPDs and leads to particularly impactful designs and results compared to conventional designs for single-band dual-polarized antennas.

V. Conclusion

In this study, a new concept and viewpoint for the design and analysis of dual-polarized antennas have been introduced. Initially, a dual-polarized antenna was devised using the CM and DM theory, which has been employed thus far for power divider design and enhancing the isolation of array antennas. By creating a slot in the radiator and connecting a metal rod, the electric field distribution was effectively altered, leading to superior isolation in the desired band. In addition, the bandwidth spanned from 3.3 to 3.8 GHz, and up to 40-dB isolation was achieved. For the target band, the gain and total efficiency were found to be 8 dBi and 90%, respectively. Furthermore, an active S-parameter and additional optimization methods for coupling tolerance were conducted to account for the effect between the two ports when used simultaneously. The proposed antenna was demonstrated to function well for the target band. Both the simulated and experimentally measured results have confirmed that the proposed antenna is an excellent candidate for wireless communication systems due to its simple configuration and low fabrication cost. In addition, this article provides the possibility to overcome a simple parametric study-based optimization.

References

[1] J. Kim and J. Oh, "Liquid-crystal-embedded aperture-coupled microstrip antenna for 5G applications," *IEEE Antennas Wireless Propag. Lett.*, vol. 19, no. 11, pp. 1958–1962, Nov. 2020.

[2] J. Seo et al., "Miniaturized dual-band broadside/endfire antenna-in-package for 5G smartphone," *IEEE Trans. Antennas Propag.*, vol. 69, no. 12, pp. 8100–8114, Dec. 2021.

[3] S. Hong, Y. Kim, and J. Oh, "Automobile laminated glass window embedded transmitarray and ray tracing validation for enhanced 5G connectivity," *IEEE Trans. Antennas Propag.*, vol. 70, no. 8, pp. 6671–6682, Aug. 2022.

[4] J. Kim, J. Kim, J. H. Oh, S.-H. Wi, and J. Oh, "Rotated feed-combined reconfigurable transmit RIS with disparate deployment of 1-bit hybrid units for B5G/6G," *IEEE Trans. Antennas Propag.*, vol. 71, no. 6, pp. 5457–5462, Jun. 2023.

[5] J. Oh, B. Kim, S. Yoon, K. Kim, E. J. Sung, and J. Oh, "High-gain millimeter-wave antenna-in-display using non-optical space for 5G smartphones," *IEEE Trans. Antennas Propag.*, vol. 71, no. 2, pp. 1458–1468, Feb. 2023.

[6] S. Wang, D. Jang, Y. Kim, and H. Choo, "Design of S/X-band dual-loop shared-aperture 2× 2 array antenna," *J. Electromagn. Eng. Sci.*, vol. 22, no. 3, pp. 319–325, 2022.

[7] G. Dong, J. Huang, S. Lin, Z. Chen, and G. Liu, "A compact dual-band MIMO antenna for sub-6 GHz 5G terminals," *J. Electromagn. Eng. Sci.*, vol. 22, no. 5, pp. 599–607, Sep. 2022.

[8] J. Cho, T. H. Lim, Y. Kim, and H. Choo, "Design of a wideband printed patch dipole antenna with a balanced on-board feeding network," *J. Electromagn. Eng. Sci.*, vol. 22, no. 6, pp. 631–637, Nov. 2022.

[9] M. O. Khalifa, A. M. Yacoub, and D. N. Aloi, "A multiwideband compact antenna design for vehicular Sub-6 GHz 5G wireless systems," *IEEE Trans. Antennas Propag.*, vol. 69, no. 12, pp. 8136–8142, Dec. 2021.

[10] A. M. A. Najafabadi, F. A. Ghani, and I. Tekin, "Low-cost multibeam millimeter-wave array antennas for 5G mobile applications," *IEEE Trans. Veh. Technol.*, vol. 71, no. 12, pp. 12450–12460, Dec. 2022.

[11] J. Zhang, K. Zhao, L. Wang, G. F. Pedersen, and S. Zhang, "Wideband low-profile dual-polarized phased array with endfire radiation patterns for 5G mobile applications," *IEEE Trans. Veh. Technol.*, vol. 70, no. 9, pp. 8431–8440, Sep. 2021.

[12] H. Wong, K. L. Lau, and K. M. Luk, "Design of dual-polarized L-probe patch antenna arrays with high isolation," *IEEE Trans. Antennas Propag.*, vol. 52, no. 1, pp. 45–52, Jan. 2004.

[13] Q.-X. Chu, D.-L. Wen, and Y. Luo, "A broadband ±45° dual-polarized antenna with Y-shaped feeding lines," *IEEE Trans. Antennas Propag.*, vol. 63, no. 2, pp. 483–490, Feb. 2015.

[14] K.-R. Xiang, F.-C. Chen, Q. Tan, and Q.-X. Chu, "High-selectivity filtering patch antennas based on MultiPath coupling structures," *IEEE Trans. Microw. Theory Techn.*, vol. 69, no. 4, pp. 2201–2210, Apr. 2021.

[15] W. Wang and Y. Zheng, "Wideband gain enhancement of a dual-polarized MIMO vehicular antenna," *IEEE Trans. Veh. Technol.*, vol. 70, no. 8, pp. 7897–7907, Aug. 2021.

[16] J. Zhu, Y. Yang, S. Li, S. Liao, and Q. Xue, "Dual-band dual circularly polarized antenna array using FSS-integrated polarization rotation AMC ground for vehicle satellite communications," *IEEE Trans. Veh. Technol.*, vol. 68, no. 11, pp. 10742–10751, Nov. 2019.

[17] Y.-M. Zhang and J.-L. Li, "A dual-polarized antenna array with enhanced interport isolation for far-field wireless data and power transfer," *IEEE Trans. Veh. Technol.*, vol. 67, no. 11, pp. 10258–10267, Nov. 2018.

[18] M. Ciydem and E. A. Miran, "Dual-polarization wideband sub-6-GHz suspended patch antenna for 5G base station," *IEEE Antennas Wireless Propag. Lett.*, vol. 19, no. 7, pp. 1142–1146, Jul. 2020.

[19] S. Yang, L. Liang, W. Wang, Z. Fang, and Y. Zheng, "Wideband gain enhancement of an AMC cavity-backed dual-polarized antenna," *IEEE Trans. Veh. Technol.*, vol. 70, no. 12, pp. 12703–12712, Dec. 2021.

[20] Z. Wang, T. Liang, and Y. Dong, "Compact in-band full duplexing antenna for sub-6 GHz 5G applications," *IEEE Antennas Wireless Propag. Lett.*, vol. 20, no. 5, pp. 683–687, May 2021.

[21] M. Li, X. Chen, A. Zhang, and A. A. Kishk, "Dual-polarized broadband base station antenna backed with dielectric cavity for 5G communications," *IEEE Antennas Wireless Propag. Lett.*, vol. 18, no. 10, pp. 2051–2055, Oct. 2019.

[22] Y. Gou, S. Yang, J. Li, and Z. Nie, "A compact dual-polarized printed dipole antenna with high isolation for wideband base station applications," *IEEE Trans. Antennas Propag.*, vol. 62, no. 8, pp. 4392–4395, Aug. 2014.

[23] Q. Xue, S. W. Liao, and J. H. Xu, "A differentially-driven dual-polarized magneto-electric dipole antenna," *IEEE Trans. Antennas Propag.*, vol. 61, no. 1, pp. 425–430, Jan. 2013.

[24] L.-H. Wen, S. Gao, Q. Luo, Q. Yang, W. Hu, and Y. Yin, "A low-cost differentially driven dual-polarized patch antenna by using open-loop resonators," *IEEE Trans. Antennas Propag.*, vol. 67, no. 4, pp. 2745–2750, Apr. 2019.

[25] Y. Li, Z. Zhao, Z. Tang, and Y. Yin, "Differentially fed, dual-band dual-polarized filtering antenna with high selectivity for 5G sub-6 GHz base station applications," *IEEE Trans. Antennas Propag.*, vol. 68, no. 4, pp. 3231–3236, Apr. 2020.

[26] L. Savy and M. Lesturgie, "Coupling effects in MIMO phased array," in *Proc. IEEE Radar Conf. (RadarConf)*, May 2016, pp. 1–6.

[27] D. M. Pozar, "A relation between the active input impedance and the active element pattern of a phased array," *IEEE Trans. Antennas Propag.*, vol. 51, no. 9, pp. 2486–2489, Sep. 2003.

[28] D. M. Pozar, *Microwave Engineering*. Hoboken, NJ, USA: Wiley, 2011.

[29] L. Sun, Y. Li, and Z. Zhang, "Decoupling between extremely closely spaced patch antennas by mode cancellation method," *IEEE Trans. Antennas Propag.*, vol. 69, no. 6, pp. 3074–3083, Jun. 2021.

[30] L. Sun, Y. Li, Z. Zhang, and H. Wang, "Antenna decoupling by common and differential modes cancellation," *IEEE Trans. Antennas Propag.*, vol. 69, no. 2, pp. 672–682, Feb. 2021.

[31] B. Qian, X. Chen, and A. A. Kishk, "Decoupling of microstrip antennas with defected ground structure using the common/differential mode theory," *IEEE Antennas Wireless Propag. Lett.*, vol. 20, no. 5, pp. 828–832, May 2021.

[32] L. Sun, Y. Li, and Z. Zhang, "Wideband decoupling of integrated slot antenna pairs for 5G smartphones," *IEEE Trans. Antennas Propag.*, vol. 69, no. 4, pp. 2386–2391, Apr. 2021.

[33] Q.-Y. Zeng, X. Zhang, L. Zhu, Q.-S. Wu, and T. Yuan, "Decoupling of antenna pairs based on equal modal conductance by antenna-shape modification," *IEEE Trans. Antennas Propag.*, vol. 71, no. 3, pp. 2182–2193, Mar. 2023.

[34] L. Sun, Y. Li, Z. Zhang, and H. Wang, "Self-decoupled MIMO antenna pair with shared radiator for 5G smartphones," *IEEE Trans. Antennas Propag.*, vol. 68, no. 5, pp. 3423–3432, May 2020.

[35] R. C. Hansen and M. Burke, "Antennas with magneto-dielectrics," *Microw. Opt. Technol. Lett.*, vol. 26, no. 2, pp. 75–78, 2000.

[36] V. G. Kasabegoudar and K. J. Vinoy, "Coplanar capacitively coupled probe fed microstrip antennas for wideband applications," *IEEE Trans. Antennas Propag.*, vol. 58, no. 10, pp. 3131–3138, Oct. 2010.

[37] C. X. Bai, Y. J. Cheng, Y. R. Ding, and J. F. Zhang, "A metamaterial-based S/X-band shared-aperture phased-array antenna with wide beam scanning coverage," *IEEE Trans. Antennas Propag.*, vol. 68, no. 6, pp. 4283–4292, Jun. 2020.

[38] S. J. Yang, Y. M. Pan, Y. Zhang, Y. Gao, and X. Y. Zhang, "Low-profile dual-polarized filtering magneto-electric dipole antenna for 5G applications," *IEEE Trans. Antennas Propag.*, vol. 67, no. 10, pp. 6235–6243, Oct. 2019.

[39] D.-Z. Zheng and Q.-X. Chu, "A wideband dual-polarized antenna with two independently controllable resonant modes and its array for base-station applications," *IEEE Antennas Wireless Propag. Lett.*, vol. 16, pp. 2014–2017, 2017.

[40] H. Huang, X. Li, and Y. Liu, "5G MIMO antenna based on vector synthetic mechanism," *IEEE Antennas Wireless Propag. Lett.*, vol. 17, no. 6, pp. 1052–1055, Jun. 2018.

Taeyeong Yoon (Graduate Student Member, IEEE) received the B.S. degree (summa cum laude) in electronic engineering from Korea Aerospace University, Goyang, South Korea, in 2021, and the M.S. degree from the Department of Electrical and Computer Engineering, Seoul National University, Seoul, South Korea, in 2023, where he is currently pursuing the Ph.D. degree.

His current research interests include suppressing dual-polarized multipath coupling, dual-polarized antennas for sub-6-GHz applications, high-efficiency power amplifiers for millimeter-wave (mm-wave) applications, and RF/mm-wave/microwave integrated circuits.

Jungsuek Oh (Senior Member, IEEE) received the B.S. and M.S. degrees from Seoul National University, Seoul, South Korea, in 2002 and 2007, respectively, and the Ph.D. degree from the University of Michigan, Ann Arbor, MI, USA, in 2012.

From 2007 to 2008, he was with Korea Telecom, Seongnam, South Korea, as a Hardware Research Engineer, working on the development of flexible RF devices. From 2013 to 2014, he was a Staff RF Engineer with Samsung Research America, Dallas, TX, USA, working as a Project Leader for the 5G/millimeter-wave antenna system. He is currently an Associate Professor with the School of Electrical and Computer Engineering, Seoul National University. He has published more than 60 technical journal articles and conference papers. His research areas include millimeter-wave (mm-wave) beam focusing/shaping techniques, antenna miniaturization for integrated systems, and radio propagation modeling for indoor scenarios.

Dr. Oh has served as a TPC Member and the Session Chair for the IEEE AP-S/USNC-URSI and ISAP. He was a recipient of the 2011–2012 Rackham Predoctoral Fellowship Award, the 2014 Samsung DMC R&D Innovation Award, the 2018 SNU Creative Researcher Award, the 2019 Samsung Electro-Mechanics Silver Prize, and the best paper awards from several conferences.